Systems/Circuits

Pathway-Specific Asymmetries between ON and OFF Visual Signals

Sneha Ravi,[1] Daniel Ahn,[2] Martin Greschner,[3] E. J. Chichilnisky,[4] and Greg D. Field[1]

[1]Department of Neurobiology, Duke University School of Medicine, Durham, North Carolina 27710, [2]Systems Neurobiology Laboratory, Salk Institute, La Jolla, California 92037, [3]Department of Biology, University of Oldenburg, 26129 Oldenburg, Germany, and [4]Departments of Neurosurgery and Ophthalmology, Stanford University, Stanford, California 94303

Visual processing is largely organized into ON and OFF pathways that signal stimulus increments and decrements, respectively. These pathways exhibit natural pairings based on morphological and physiological similarities, such as ON and OFF α-ganglion cells in the mammalian retina. Several studies have noted asymmetries in the properties of ON and OFF pathways. For example, the spatial receptive fields (RFs) of OFF α-cells are systematically smaller than ON α-cells. Analysis of natural scenes suggests that these asymmetries are optimal for visual encoding. To test the generality of ON/OFF asymmetries, we measured the spatiotemporal RF properties of multiple RGC types in rat retina. Through a quantitative and serial classification, we identified three functional pairs of ON and OFF RGCs. We analyzed the structure of their RFs and compared spatial integration, temporal integration, and gain across ON and OFF pairs. Similar to previous results from the cat and primate, RGC types with larger spatial RFs exhibited briefer temporal integration and higher gain. However, each pair of ON and OFF RGC types exhibited distinct asymmetric relationships between RF properties, some of which were opposite to the findings of previous reports. These results reveal the functional organization of six RGC types in the rodent retina and indicate that ON/OFF asymmetries are pathway specific.

Key words: cell types; classification; retina

Significance Statement

Circuits that process sensory input frequently process increments separately from decrements, so-called ON and OFF responses. Theoretical studies indicate that this separation, and associated asymmetries in ON and OFF pathways, may be beneficial for encoding natural stimuli. However, the generality of ON and OFF pathway asymmetries has not been tested. Here we compare the functional properties of three distinct pairs of ON and OFF pathways in the rodent retina and show that their asymmetries are pathway specific. These results provide a new view on the partitioning of vision across diverse ON and OFF signaling pathways.

Introduction

The division of sensory signals across neurons that respond to stimulus increments (ON) or decrements (OFF) is a common processing motif. Examples abound, as follows: olfactory receptor neurons in the cockroach respond to either increments or decrements in odor concentration (Burgstaller and Tichy, 2011); neurons in auditory cortex respond to increments or decrements of sound intensity (Scholl et al., 2017); neurons in the fish electrosensory system signal increasing or decreasing contrasts in amplitude modulations of an electromagnetic field (Berman and Maler, 1998; Clarke et al., 2014); and neurons from retina to visual cortex respond to increments or decrements of light intensity (Hartline, 1938; Hubel and Wiesel, 1962). Thus, understanding how and why ON and OFF pathways partition sensory input is central to an understanding of sensory processing.

In vision, the division of sensory processing between ON and OFF pathways is elaborate. The division originates at the first retinal synapse between photoreceptors and bipolar cells. Within one additional synaptic layer, the retina partitions visual scenes into 30–40 different channels, each instantiated by a distinct retinal ganglion cell (RGC) type (Field and Chichilnisky, 2007; Sanes and Masland, 2015). Many of these RGC types respond to either increments or decrements of light in their receptive field (RF) center (Hartline, 1938; Kuffler, 1953; Wässle and Boycott,

Received Aug. 6, 2018; revised Sept. 8, 2018; accepted Sept. 12, 2018.

Author contributions: E.J.C. and G.D.F. designed research; S.R., D.A., M.G., and G.D.F. performed research; S.R., D.A., and G.D.F. analyzed data; G.D.F. wrote the paper.

This research was supported by National Institutes of Health/National Eye Institute Grants R01-EY-024567 (to G.D.F.), R01-EY-021271 (to E.J.C.), R01-EY-017992 (to E.J.C.), and P30-EY-019005 (to E.J.C.); and by the Karl Kirchgessner Foundation (to G.D.F); the Whitehall Foundation (to G.D.F); and the Whitehead Scholars Program (to G.D.F). We thank Jon Cafaro, Lindsey Glickfeld, Fred Rieke, and Kiersten Ruda for comments on the manuscript; and Teleza Westbrook, Alexander Sher, and Alan M. Litke for technical support.

The authors declare no competing financial interests.

Correspondence should be addressed to Dr. Greg D. Field, Department of Neurobiology, 311 Research Drive, Duke University, Durham, NC 27710. E-mail: field@neuro.duke.edu.

https://doi.org/10.1523/JNEUROSCI.2008-18.2018

 0270-6474/18/389728-13$15.00/0

1991). Furthermore, many of these ON and OFF RGC types form pairs, such as ON and OFF α-cells in cats and other mammals (Cleland and Levick, 1974; Cleland et al., 1975; Watanabe and Rodieck, 1989; Wässle and Boycott, 1991). These pairings have been established on both morphological and functional grounds. Morphologically, these pairs have dendritic fields that are similar in size and branching patterns, but that ramify in different depths of the inner plexiform layer (Wässle and Boycott, 1991; Dacey, 2004). Functionally, these pairs exhibit similar receptive fields with a polarity reversal. However, more recent multineuron measurements have identified systematic "asymmetries" between some paired ON and OFF RGC types (Chichilnisky and Kalmar, 2002; Ratliff et al., 2010). For example, ON parasol RGCs exhibit larger spatial RFs than their OFF-cell counterparts. Asymmetries between ON and OFF pathways have also been observed in temporal integration, contrast response functions, absolute sensitivity, nonlinear spatial integration, and adaptation (Chichilnisky and Kalmar, 2002; Nirenberg et al., 2010; Pandarinath et al., 2010; Ala-Laurila and Rieke, 2014; Turner and Rieke, 2016). This has led to an evolving view of how ON and OFF pathways are organized with respect to one another. In particular, ON and OFF pairs exist, but their differences may extend beyond a flip of polarity.

These asymmetries have been studied mostly in α and parasol RGCs, which are probably homologs (Crook et al., 2008a). This raises the question, how ubiquitous are these asymmetries? Analysis of natural scenes suggests that RF size asymmetries may be an efficient coding scheme for natural scenes (Ratliff et al., 2010; Barlow, 1961; Pandarinath et al., 2010; Karklin and Simoncelli, 2011). These results suggest asymmetries may be preserved across ON and OFF pathway pairs. However, these analyses were agnostic to the particular aspects of the visual image represented by distinct cell types, which may dictate distinct asymmetries (or even symmetry) for efficient coding.

The goal of this study was to measure the organization of RFs across multiple pairs of ON and OFF RGCs to determine the extent to which asymmetries are general or pathway specific. We measured the RF properties of hundreds of simultaneously recorded rat RGCs using a multielectrode array. We developed a procedure for functionally classifying RGCs based on their responses to diverse visual stimuli. This classification yielded six irreducible cell types − three pairs of ON and OFF RGC types. Across three pairs of ON and OFF RGCs from these six types, we found that the relative organization and the presence of functional asymmetries was pathway dependent. Each pair exhibited a distinct set of asymmetries in spatiotemporal integration and contrast response functions. These results indicate that asymmetries between ON and OFF pairs are common, but that the differences between pairs vary with the cell type and their light response properties.

Materials and Methods

Tissue preparation and multielectrode array recordings

All experiments followed procedures approved by the Institutional Animal Care and Use Committee of Duke University and the Salk Institute for Biological Studies. Long–Evans rats were killed by intraperitoneal injection of ketamine and xylazine. Retinas were removed in darkness under infrared illumination with infrared converters, as described previously (Anishchenko et al., 2010; Yu et al., 2017). An ~1.5 × 3 mm segment of dorsal retina, centered 3.5–4 mm above the optic nerve and ±1 mm along the vertical meridian, was isolated. This region of retina was targeted to minimize variability across experiments and to target retinal locations with cones expressing mostly M-opsin. The retina was placed with the RGC side down on an electrode array consisting of 512 electrodes with 60 μm interelectrode spacing, spanning an area of 0.9 × 1.8 mm (Litke et al., 2004). The voltage trace recorded on each electrode was bandpass filtered between 80 and 2000 Hz, sampled at 20 kHz, and stored for off-line analysis (Frechette et al., 2005). Spikes were initially sorted by an automated algorithm, and the resulting clusters were checked and corrected manually using custom spike-sorting software (Shlens et al., 2006; Yu et al., 2017). The autocorrelation function of sorted spikes was used to validate putative RGCs by checking for a refractory period (1.5 ms; Field et al., 2007). To track the RGCs across different visual stimuli, spike shapes were sorted in the same subspace determined by principal components analysis (PCA) of the spike waveforms. Neuron identity was further confirmed across different stimuli by checking that the electrical image (EI; Petrusca et al., 2007) for each neuron matched across conditions. A matched neuron between two stimulus conditions was determined by the EI pair with the highest inner product across the two stimulus conditions (Field et al., 2009). A typical experiment resulted in recording and tracking the responses of 300–400 RGCs across three visual stimuli.

Visual stimuli and RGC response properties

Visual stimuli from a gamma-corrected CRT video display (Trinitron, Sony) refreshing at 120 Hz, or an organic light-emitting diode display (Emagine) refreshing at 60 Hz, were focused on the retina via an inverted microscope (Yu et al., 2017). Three different stimuli were used to measure the functional properties of recorded RGCs (Fig. 1*A*); each was photopic with a mean intensity of either 3000 or 10,000 photoisomerizations/rod/s (Field et al., 2009; Yu et al., 2017). First, a checkerboard noise stimulus was used to estimate the spatiotemporal RF by reverse correlation (Chichilnisky, 2001). Each checker of the noise stimulus was 40 × 40 μm on the retina and noise images were updated at 60 Hz. Second, sine wave gratings with a spatial period of 320 μm on the retina were drifted in eight directions at two speeds (150 and 600 μm/s). This stimulus identified RGCs that were sensitive to motion (Fig. 2*A*; Yu et al., 2017). Finally, in a subset of experiments (four of seven), full-field light steps were presented to the retina. This stimulus consisted of a full-field change in light intensity that switched every 2 or 3 s from gray (50% monitor output) to white (100%), to gray to black (1%), and back to gray. This stimulus cycled through this progression 25 times, and peristimulus time histograms (PSTHs) were generated from the responses of the recorded RGCs (Fig. 1; see Fig. 5).

RGC classification

RGCs from seven retinas were classified in this study. The number of cells identified for each cell type in each retina are provided in Table 1. The classification approach consisted of the following two stages: a feature selection process followed by a serial, quantitative classification using unsupervised learning. The feature selection process identified response properties that robustly isolated one or a small number of RGC types from all other types [e.g., isolating direction-selective (DS)-RGCs from non-DS-RGCs; Fig. 2*A*]. The quantitative classification clustered neurons using these features by a two-Gaussian mixture model (GMM).

Stage one. The feature selection process was performed using one of the seven retina recordings in this manuscript. This stage was used to identify response parameters that distinguished one set of RGCs from all others. In this initial dataset, high-dimensional data were parameterized and visualized in a lower dimensional space by PCA. These spaces consisted of either two or three dimensions, each defined by a response parameter such as the overall spike rate or the shape of the temporal RF (Fig. 2*C*). Limiting the dimensionality facilitated robust clustering of RGCs with relatively limited data (e.g., a few hundred RGCs). Once a set of response features was identified that clearly separated one group of RGCs from the others, the spatial RFs of the grouped RGCs were inspected to check whether they were regularly spaced. If grouped RGCs were regularly spaced, the features used were saved for quantitative clustering (see stage two). Performing feature selection before quantitative classification improved the performance of the unsupervised clustering algorithm by minimizing misclassification rates.

Stage two. To quantitatively cluster each group of RGCs (Fig. 2), a two-GMM was fit to the same two- or three-dimensional feature space

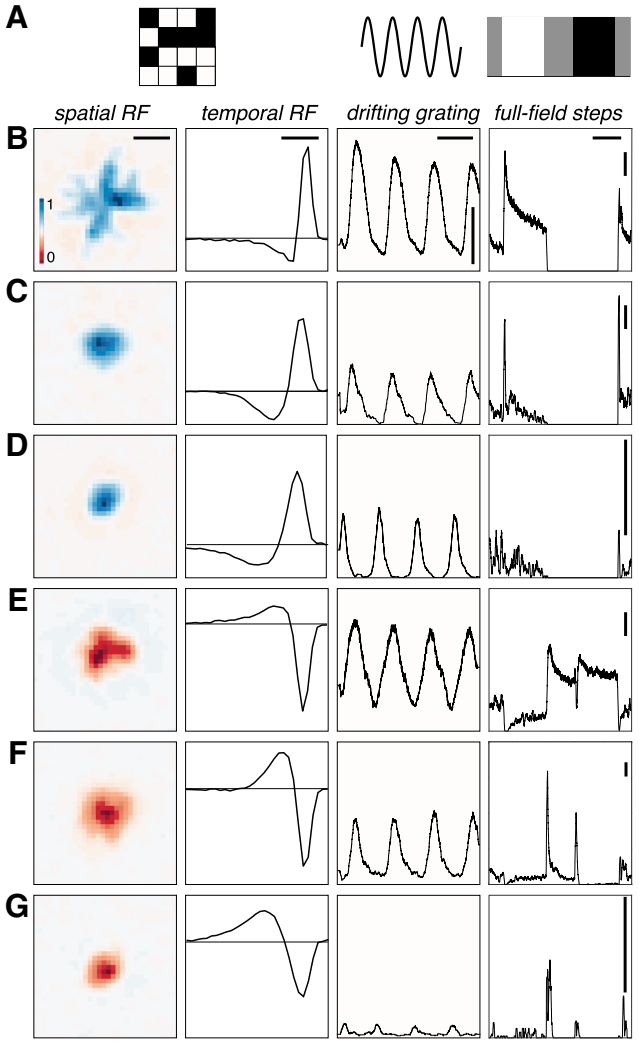

Figure 1. Example RGCs with diverse receptive fields and light response properties. ***A***, Illustrations of the three stimuli used in this study: checkerboard noise, drifting gratings, and full-field steps of light intensity. ***B***, Receptive fields and responses of an example RGC. From left to right: Spatial RF; scale bar, 320 μm. Temporal RF: calibration, 120 ms. PSTH from responses to eight presentations of a drifting grating (spatial period, 320 μm; temporal period, 2 s). calibration: horizontal bar, 2 s; vertical bar, 20 Hz. PSTH from 25 response full-field light steps that cycle from gray (2 s) to white (3 s) to gray (2 s) to black (3 s) every 10 s. Calibration: horizontal bar, 2 s; vertical bar, 20 Hz. ***C–G***, Same as ***A*** from different RGCs. Scales are constant in each column, unless the calibration bar is redrawn (e.g., right column), in which case the calibration value remains constant. Note that each RGC is at a different location on the MEA and is subject to a different phase of the drifting grating, causing the phase relationships across cells to be arbitrary.

defined above in stage one. The GMM allowed boundaries to be drawn between clusters according to the maximum likelihood that RGCs belonged to one Gaussian distribution or the other. RGC types were classified one at a time in a serial fashion to prevent overfitting and avoid ambiguity in choosing the right number of clusters. Each cluster was tested for statistical significance (Tukey's range test), and the irreducibility of each type was verified by testing for a mosaic organization (see Fig. 4). The order of this serial classification and the response parameters that consistently identified RGCs across recordings is shown in Figure 2.

Verifying RGC types

Clustered RGCs were identified as an irreducible cell type by inspecting the normalized nearest neighbor distribution (NNND; see Fig. 4; DeVries and Baylor, 1995; Field et al., 2007). The NNND is defined as $2R/(S1 + S2)$. R is the distance between the spatial RF of each RGC and the RF of its nearest neighbor. $S1$ and $S2$ are SDs of the Gaussian fits for the spatial RF of each RGC measured along the line connecting the centroids. If the two spatial RFs "touch" at the 1 SD contour for each cell, then the NNND will equal 2.

NNNDs indicate a mosaic-like arrangement of RFs when they exhibit a clear exclusion zone at short nearest-neighbors at distances (Wässle and Riemann, 1978). To test the null hypothesis that the observed NNND were consistent with a random sampling of RGCs, we generated 100 NNND distributions from randomly sampled RGCs within each experiment (see Fig. 4*A*). The number of sampled cells equaled the number of RGCs in the original mosaic. A two-sample Kolmogorov–Smirnov test was used to estimate the probability that the observed NNND was consistent with that expected from a randomly sampled set of RGCs. In 38 of 42 mosaics tested, the null hypothesis was rejected with $p < 0.05$ (see Fig. 4*B*).

Estimation of linear spatiotemporal RFs

A linear approximation to the spatiotemporal RF of each RGC was obtained by reverse correlation to compute the spike-triggered average (STA; Chichilnisky, 2001). Frames up to 500 ms preceding a spike were included in the analysis. The spatial RF was the set of stimulus pixels (stixels) whose absolute peak intensity exceeded 4.5 robust SDs of all pixel intensities (Yu et al., 2017). The temporal RF was defined as the time-dependent average of these significant stimulus pixels. Once the temporal RF was computed, the dot product between every stixel of the STA was computed with the temporal RF. This collapsed the STA across time to a single image, which was used as an estimate of the spatial RF.

This analysis to extract estimates of the spatial and temporal RFs assumes the spatiotemporal RF is separable into a single spatial and temporal filter. The validity of this assumption was examined using singular value decomposition (SVD; Golomb et al., 1994). SVD factorizes a matrix into a rank-ordered set of vector pairs whose outer products are weighted and linearly combined to reproduce the original matrix. A perfectly space-time separable RF will produce a single pair of nonzero vectors capturing the spatial and temporal RFs, respectively. Before performing SVD, a Gaussian spatial filter was applied to the full spatiotemporal RF to reduce noise in the STA. This Gaussian filter was circular with an SD of 0.75 stixels. After applying this filter, SVD indicated that across cell types, >90% of the variance in the STA could be captured by the outer product of a single pair of spatial and temporal filters. This indicates that the linear RF structure was largely consistent with a space—time-separable model.

Space–time plots

To generate average space–time plots of RGC RFs (see Fig. 7), the entire spatiotemporal RF was filtered for each cell with a circular Gaussian filter (SD = 0.75 stixels). A 21 × 21 stixel (924 × 924 μm) region around the center of mass of the spatial RF was cropped. The average 3-dimensional spatiotemporal RF of each RGC type was computed by averaging together all the cropped and filtered spatiotemporal RFs of all cells of that type across all recordings. The 3-dimensional spatiotemporal RF was collapsed to 2 dimensions by extracting the intensities along one spatial axis.

Estimation of contrast response functions

Contrast response functions were estimated from the static nonlinearity (SNL) computed by convolving the spatiotemporal RFs with the checkerboard noise stimulus (Chichilnisky, 2001). This yielded an instantaneous generator signal for each frame of the stimulus that was used to generate a histogram of observed spike counts for each generator signal. This histogram was fit with a logistic function. The slope (b) and offset (a) were parameters from the logistic function fit to the SNL: $(c/(1 + \exp(-b(x - a)))$. To check that the static nonlinearity was accurately fit, simulated spikes were generated from a model linear-nonlinear Poisson neuron in response to a checkerboard white noise stimulus. A logistic function was used in the simulation for the nonlinearity. When total spike counts were matched between simulated and real neurons, the model fitting produced estimates of the slope and offset within 1% of the values set in simulation. We also checked that the distribution of stimuli preceding spikes exhibited a unimodal projection onto the STA: ON and

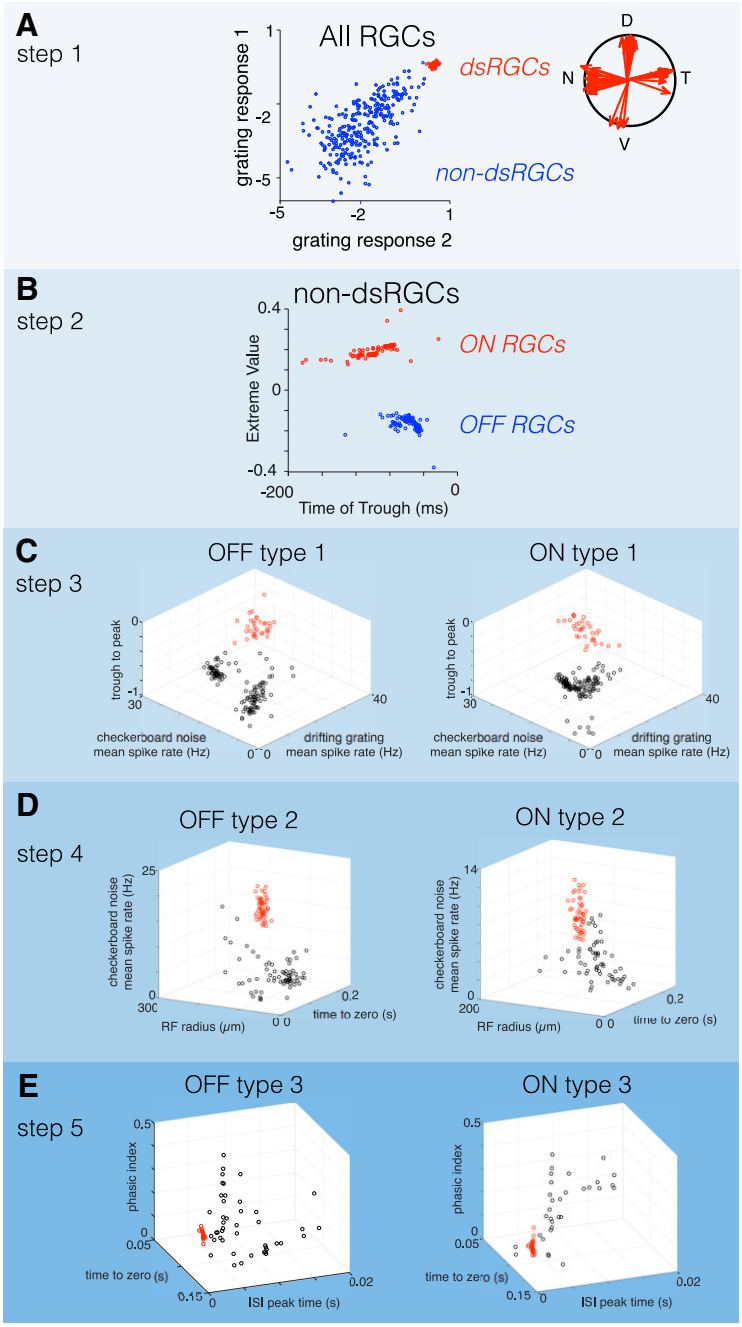

Figure 2. Serial classification of RGCs yielded three pairs of ON and OFF cells. ***A***, In step 1 of the classification, DS-RGCs are segregated from all other cells based on their responses to drifting gratings. Grating responses 1 and 2 are the log [base 2] of the vector magnitude to a grating with a spatial period of 320 μm drifting at 150 and 600 μm/s, respectively. Gratings were drifted in eight directions to estimate the vector magnitudes of their tuning. ***B***, In step 2, ON and OFF RGCs were segregated by the value of the extrema, and the time to trough of their temporal RFs were estimated from their STA. ***C***, In step 3, a pair of ON and OFF RGCs (red points) were classified from all other ON and OFF cells, respectively. The parameter spaces used to classify these two types were identical and consisted of the mean spike rates in response to checkerboard noise (stixel size, 40 × 40 μm; 60 Hz refresh) and a drifting grating (spatial period, 320 μm; speed, 150 μm/s), as well as the trough-to-peak ratio of their temporal RFs. ***D***, In step 4, ON and OFF RGCs identified in step 3 were removed, and the remaining ON and OFF RGCs were classified in a new parameter space defined by the mean spike rate to checkerboard noise, RF radius, and the time to zero of the temporal RF. ***E***, In step 5, ON and OFF RGCs identified in the two previous steps were removed, and the remaining ON and OFF cells were classified in a new parameter space defined by the phasic index (estimated from the temporal RF; see Materials and Methods), the time to zero of the temporal RF, and the peak time of the ISI distribution. At each step of the classification, groups of cells were distinguished by a two-Gaussian mixture model.

OFF cells will exhibit this property, whereas ON-OFF cells will exhibit a bimodal projection. For every cell of each of the six types of cells analyzed in this study, this projection was unimodal and was well approximated by a Gaussian distribution.

Accuracy of the linear-nonlinear-Poisson model

An important caveat in the RF measurements presented here is that they are linear estimates. These estimates have been shown in some circumstances to accurately capture the stimulus features that drive RGC spiking (Chichilnisky, 2001; Keat et al., 2001; Pillow et al., 2005). However, for some RGC types, stimulus features interact nonlinearly in space and/or time (Hochstein and Shapley, 1976; Schwartz et al., 2012; Freeman et al., 2015). To determine the capacity of these linear RF estimates and contrast response functions to capture the relationship between the stimulus and spiking, we cross-validated the model to a repeated checkerboard noise stimulus in a subset of experiments (Table 1, retinas 2 and 3). A 10 s checkerboard noise sequence (40 × 40 μm stixels, 60 Hz refresh) was repeated 100 times. For a given RGC, the linear-nonlinear-Poisson (LNP) model generated from the spatiotemporal RF and the static nonlinearities estimated from the nonrepeating checkerboard noise were used to predict the response to the repeated checkerboard stimulus (not used in the original estimate of the STA or static nonlinearity). Across cells of all six types, spike trains generated by the LNP model captured 51–73% of the explainable variance (data not shown).

Parameterizing stimulus responses

Vector sum for drifting gratings. The total spike count from RGCs to eight presentations of a grating drifting in each of eight directions was calculated and normalized by the maximum count. This yielded eight vectors that had magnitudes ranging between 0 and 1. The sum of these vectors identified the preferred direction of the RGC (Elstrott et al., 2008; Rivlin-Etzion et al., 2012), and the magnitude of this vector was used to estimate the strength of tuning and classify DS-RGCs from non-DS-RGCs in Figure 2*A*. The vector sum was not normalized to 1 to allow the vector magnitude to range from zero to infinity. This allowed the Gaussian mixture model to be fit to the log (base 2) of the vector sum: these distributions were approximately log-normal.

Firing rate for drifting gratings and checkerboard noise. The firing rates in response to drifting gratings were calculated by dividing the total spike count by the number of stimulus repeats (8) and directions (8), and the length of time that the grating was presented to the retina (8 or 10 s). For checkerboard noise, the total number of spikes during the presentation of the checkerboard noise was divided by the total time.

Parameters of the temporal RF from checkerboard stimuli. The time to peak and time to trough were taken from the global maximum and minimum, respectively, in the temporal RF. The zero crossing was calculated as the time closest to the spike at which the temporal RF transitioned from positive to negative values for OFF cells and vice versa for ON cells. The maximum and minimum values were taken as the global maximum and minimum in the temporal RF, respectively. A phasic index (PI) was calculated from the temporal RF as the absolute value of the sum of the

Table 1. RGC counts are provided for the six RGC types identified and examined across the seven retinal recordings used in this study

	Retina						
RGCs	1	2	3	4	5	6	7
ON brisk sustained	33	24	20	26	22	25	38
ON brisk transient	51	40	50	39	48	53	37
ON small transient	28	20	23	20	21	30	9
OFF brisk sustained	34	27	26	31	33	33	23
OFF brisk transient	52	30	44	36	37	40	48
OFF small transient	15	10	7	10	14	21	12

positive and negative areas divided by the sum of their absolute values (e.g., $|(a + b)|/(|a| + |b|)$). The PI ranges from zero to one: zero corresponds to a biphasic temporal RF, with the area above and below zero being equal; one corresponds to a monophasic temporal RF. The biphasic index (see Fig. 8*D*) equaled 1 − PI (Petrusca et al., 2007).

Parameters of the spatial RF from checkerboard stimuli. The spatial RF diameter (see Fig. 8*A*) was defined as the diameter of a circle with the same area as the 1 SD boundary of a two-dimensional Gaussian fit to the RF center (Chichilnisky and Kalmar, 2002; Gauthier et al., 2009). To plot the spatial RF mosaics (Fig. 3*A*, *D*), RFs were filtered by convolving with a two-dimensional Gaussian filter with an SD of 0.75 stixels. Contour lines were then linearly interpolated in each RF using a fixed contour equivalent to 1 SD, 0.6065 of the peak (Yu et al., 2017).

Results

Multielectrode array (MEA) measurements from rat retinas yield RGCs with diverse response properties. Checkerboard noise, drifting gratings, and full-field light steps illustrate some axes along which RGC responses vary (Fig. 1). As illustrated in numerous previous studies, RGCs exhibit ON versus OFF responses (Fig. 1, compare *B–D*, *E–G*), differences in spatial and temporal receptive fields (Fig. 1*B–G*, two left columns), transient versus sustained responses (Fig. 1, compare *B–D*, *C–E*), and differences in the number of spikes elicited to gratings and full-field changes in light (Fig. 1*B–G*, two right columns; Kuffler, 1953; Cleland and Levick, 1974; Caldwell and Daw, 1978; Wässle and Boycott, 1991). In the following sections, we show the results of a functional classification applied to the responses of rat RGCs recorded on a large-scale MEA. This classification yields a natural set of three pairings between ON and OFF RGC types. We analyze the spatiotemporal RF properties and gain among these six cell types and compare the results across ON and OFF pairs.

The rat retina contains at least three functional pairs of ON and OFF cells

To analyze the RF structure and gain across cell types, we took a serial approach to classifying RGCs (see Materials and Methods). In the first step, DS-RGCs were separated from other cells based on their responses to gratings drifting in different directions and at different speeds (Fig. 2*A*). In the second step, non-DS-RGCs were split into cells with stronger ON or OFF responses (Fig. 2*B*). The dominant response polarity was determined from the STA to a checkerboard stimulus (see Materials and Methods). In the third, fourth, and fifth steps, ON and OFF RGCs were serially classified by identifying a small number of response parameters that clustered RGC types. These response parameters included information about the mean firing rates, RF size, and duration/kinetics of temporal integration. This approach yielded three ON and three OFF RGC types.

Across these six RGC types, the classification approach indicated a natural set of three pairs of ON and OFF cell types. For ON and OFF types to be paired, they must resemble one another more than they resemble other cell types, either morphologically (Wässle et al., 1981a) or functionally (Devries and Baylor, 1997). This kind of similarity was indicated by two observations. First, the parameter spaces used to classify ON and OFF RGCs were the same for each pair (Fig. 2*C–E*, steps 3–5). Second, the relative distribution of cells within those parameter spaces was similar for each pair. These two features ensured that the same response properties segregated each pair from all other recorded ON and OFF cells and did so in a similar fashion. These are the core criteria for defining an ON and OFF signaling pair.

The first pair of ON and OFF RGCs (Fig. 2*C*, step 3) was distinguished by their mean spike rate in response to a drifting grating, the mean response to checkerboard noise, and the ratio between the trough and peak of their temporal RFs. A low trough-to-peak ratio indicates relatively monophasic temporal integration and "sustained" responses to steps of light. Thus, this first pair of ON and OFF cells exhibited the highest firing rates to drifting gratings and checkerboard noise, relatively sustained responses, and weakly biphasic temporal integration.

After removing this first pair of classified cells, the second pair of ON and OFF RGCs was classified in a new parameter space that compared spatial RF size, duration of temporal integration (time-to-zero), and the mean spike rate to checkerboard noise (Fig. 2*D*). For both ON and OFF RGCs, groups of cells exhibited high firing rates in response to checkerboard noise stimuli, large RFs, and brief temporal integration.

In the final classification step (Fig. 2*E*), the remaining unclassified RGCs were compared in a parameter space consisting of the time to zero of the temporal RF, a phasic index calculated on the temporal RF (see Materials and Methods), and the time of the peak in the interspike interval (ISI) distribution. Clusters of ON and OFF cells emerged in these spaces with the briefest ISI peaks, relatively biphasic temporal RFs, and long time-to-zero crossings.

These classification results indicated a set of pairings between ON and OFF RGCs among the cells identified in our MEA measurements. In the subsequent section, we examine whether these cells form irreducible types and compare their response properties across a broader range of parameters.

Each identified ON and OFF cell type forms a mosaic

A hallmark of cell types in the retina is that they tile space morphologically with dendritic fields and functionally with spatial RFs (Wässle and Riemann, 1978; Wässle et al., 1981b; Dacey, 1993; Devries and Baylor, 1997; Novelli et al., 2005; Field and Chichilnisky, 2007). Thus, we tested whether the clusters of ON and OFF cells identified in our serial classification tiled space to form a mosaic-like pattern with their spatial RFs. We measured RGC spatial RFs from STAs in response to checkerboard noise (see Materials and Methods; Chichilnisky, 2001; Yu et al., 2017). Plotting the spatial RFs for each RGC type revealed that all six types exhibited a mosaic-like organization (Fig. 3*A*, *D*). An analysis of the nearest neighbor distributions for RGCs of each type revealed nonrandom spatial RF organizations for each type across most retinas (Fig. 4). Importantly, no information about the spatial locations of cells was explicitly contained in the response parameters used to distinguish cell types. Thus, the observation of mosaics is a validation that the classification yielded irreducible cell types.

Another feature of RGC types is that response parameters should vary less within a type than across types. Thus, we checked that the temporal RFs (reflecting the temporal integration of vi-

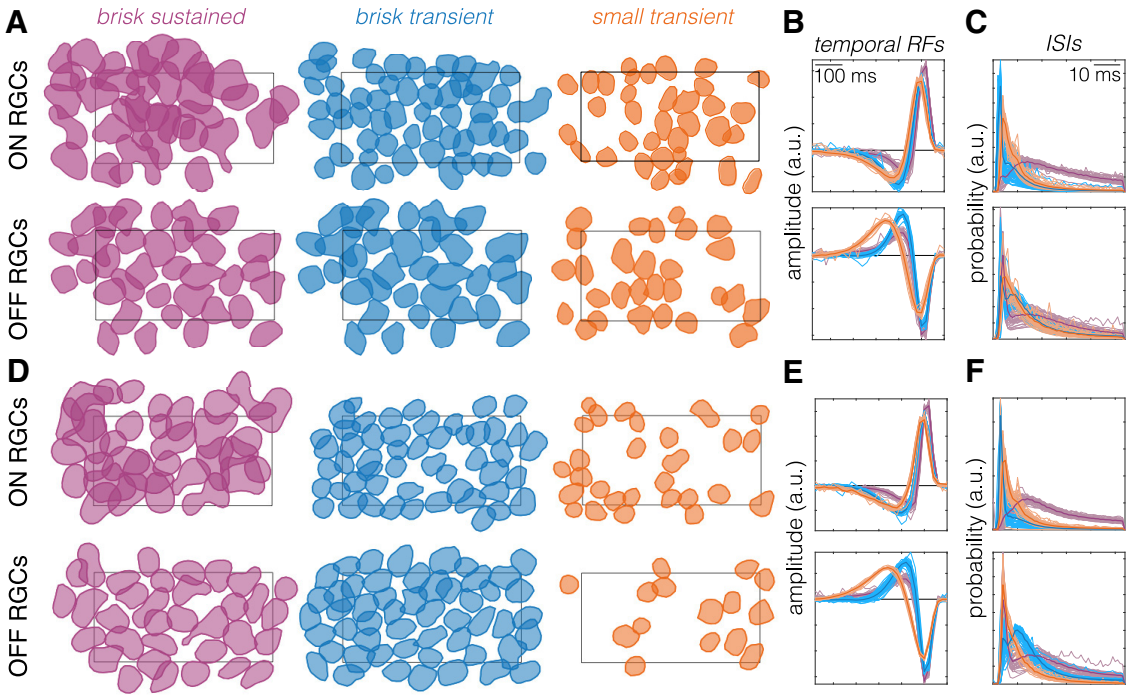

Figure 3. Classified ON and OFF RGCs exhibit a mosaic-like organization. ***A***, Spatial RFs of ON and OFF brisk sustained (purple), brisk transient (blue), and small transient (orange) RGCs identified in one retina. Spatial RFs are shown as a contour plotted at 0.6065 of the peak amplitude (equivalent to 1 SD of Gaussian). The rectangle shows the outline of the MEA (900 × 1800 μm). ***B***, Temporal RFs of all cells shown in ***A***, with ON cells on top and OFF cells on bottom. Thin lines are individual cells, thick lines are the mean. Color conventions are the same as in ***A***. ***C***, ISI distributions for all cells in ***A***. Color and line conventions same as in ***A*** and ***B***. ***D–F***, Same as ***A–C***, but for a second retina.

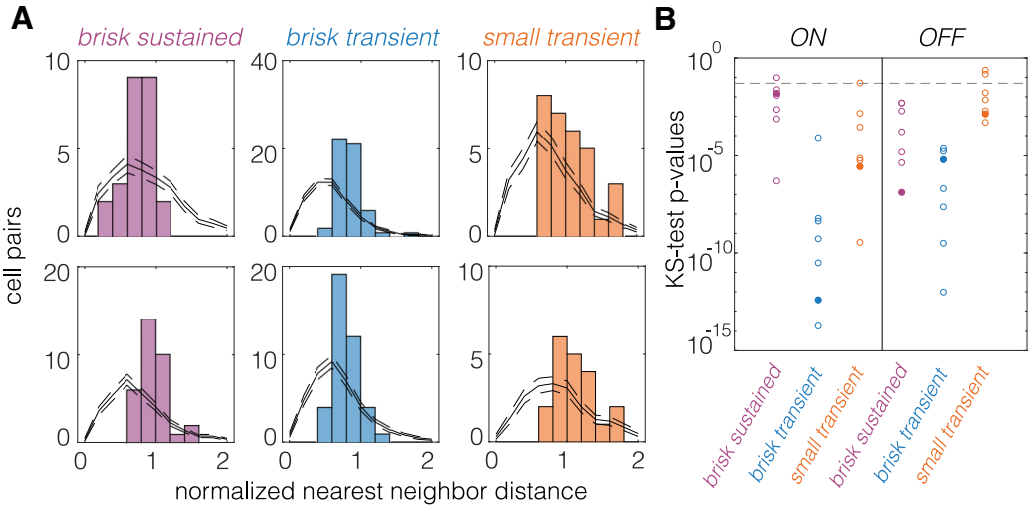

Figure 4. NNNDs indicate a mosaic-like arrangement of spatial RFs. ***A***, NNNDs for brisk sustained, brisk transient, and small transient cells, with ON cells at the top and OFF cells at the bottom. Data are from one retina. Black lines show expected NNNDs for randomly sampled cell locations (see Materials and Methods); dashed lines show the 95% CI. ***B***, *p* Values from a two-sample Kolmogorov–Smirnov (KS) test for observed NNNDs arising from random cell locations. Fill circles correspond to the data shown in ***A***.

sual input) were more similar within a type than across types. Temporal RFs were measured from the STA time courses in response to checkerboard noise (see Materials and Methods). Plotting the temporal RFs for all six types revealed highly stereotyped temporal integration within a type and distinct temporal integration across types (Fig. 3*B*,*E*). Finally, we compared (ISI) distributions across types. The ISIs reflect the spiking dynamics of each RGC. Similar to the temporal RFs, the ISI distributions were more similar within a type than across types for both ON and OFF RGCs (Fig. 3*C*,*F*).

These features of the six RGC types supported the conclusion that each represented an irreducible cell type. Henceforth, we refer to the first pair of classified RGCs (Fig. 2*C*) as ON and OFF brisk sustained RGCs based on their short latency, sustained responses to visual stimuli, and previously used naming conventions (Caldwell and Daw, 1978; Devries and Baylor, 1997; Girman and Lund, 2010; Heine and Passaglia, 2011). Similarly, we refer to the second and third pairs of classified RGCs (Fig. 2*D*,*E*) as brisk transient and small transient RGCs, respectively.

Distinctions across types persist when tested with alternative stimuli

We also examined the responses to a stimulus not used in the classification, presented in a subset of recordings. This stimulus consisted of full-field steps of light that cycled through transitions from gray to white to gray to black and back to gray every few seconds (see Materials and Methods). The PSTHs from responses to this stimulus were distinct between the identified cell types, and the within-type variability was small relative to the between-type variability (Fig. 5; see also Yu et al., 2017). Furthermore, the PSTHs confirm that each type is dominated by either an ON or an OFF response; these are not ON-OFF cells under the photopic conditions of this study.

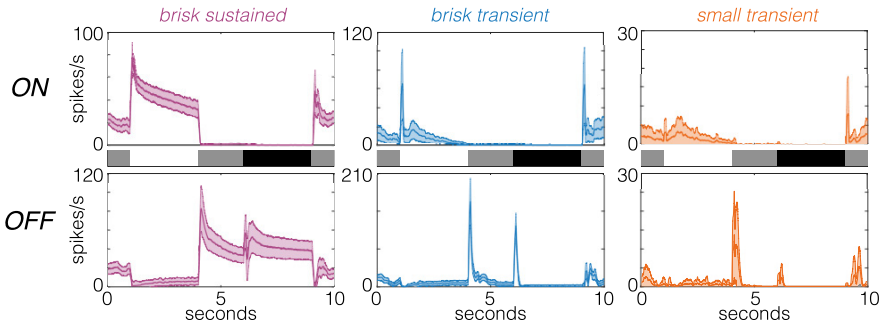

Figure 5. Responses to full-field light steps are distinct across the identified cell types. Average PSTHs of field light steps for six cell types. Shaded regions show the SD. The timing of transitions from gray to white to gray to black are shown in the stimulus traces between the top (ON cells) and bottom (OFF cells) rows. Cell numbers for each type are given in Table 1 (retina 2).

Naive clustering supports pairing these ON and OFF types

To test whether the pairings of these types were warranted, we compared the temporal RFs across all six RGC types in a reduced dimensional space defined by PCA. ON and OFF brisk sustained cells clustered together after accounting for their difference in response polarity (Fig. 6*A*,*B*). Similarly, ON and OFF brisk transient and ON and OFF small transient cells were more similar to one another, respectively, than to the other identified types. To test that this particular set of pairings was objectively the best three-group association across all six types, we fit a three-Gaussian mixture model to the data, using the first five PCs (Fig. 6*C*,*D*). The Gaussian mixture model produced an exact match to the three-group description produced by combining ON and OFF cells across brisk sustained, brisk transient, and small transient cells (Fig. 6, compare *A*, *C*, compare *B*, *D*). This further supports the functional pairings established in the serial classification (Fig. 2).

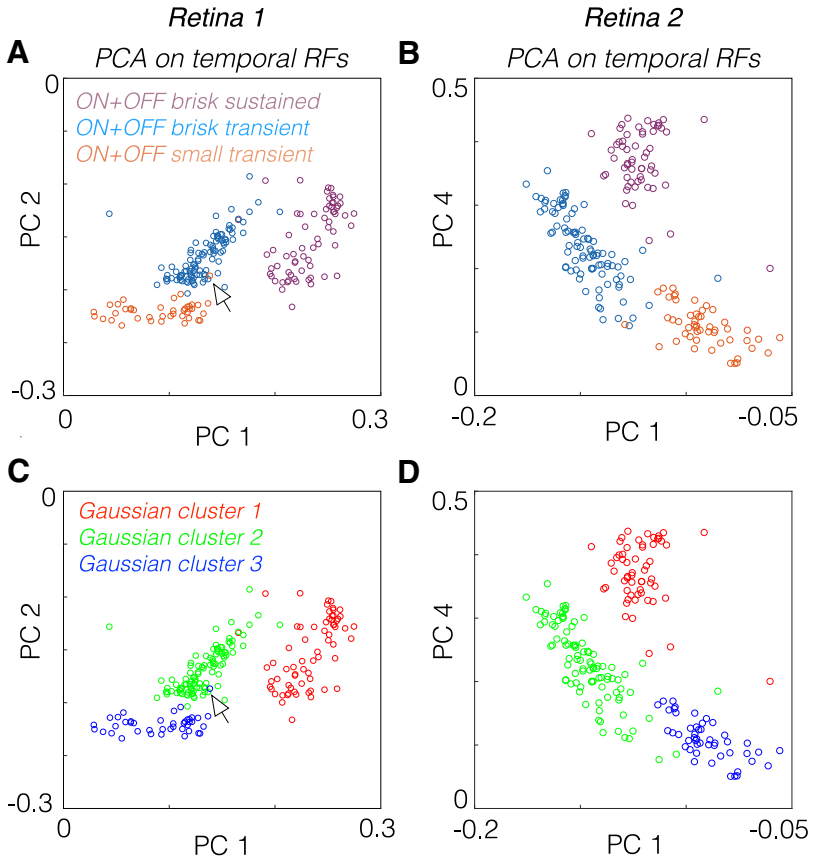

Figure 6. Temporal RFs of ON and OFF pairs cluster together after accounting for polarity differences. ***A***, PCA applied to the temporal RFs of brisk sustained, brisk transient, and small transient cells from one experiment. The temporal RFs of OFF cells were multiplied by −1 to invert their polarity before PCA. Each circle represents one RGC, and circles were colored by the cell type determined by the classification in Figure 1. ***B***, Same analysis as in ***A***, but for a second retina and weights associated with PC 4 are plotted instead of PC 2. ***C***, Same data as in ***A***, but a three-Gaussian mixture model was fit to the data in the space defined by the first five principal components, which captured >99% of the variance in the data. ***D***, Same as ***C***, but for a second retina. This fit finds the best three-group description of the data (provided that each group is well described by a multivariate Gaussian distribution). The Gaussian mixture model clustered the temporal RFs identically to the groupings defined by combining ON and OFF pairs together. Even points that appear outside of their appropriate group (see arrowheads) in the two-dimensional plot are correctly classified by the Gaussian mixture model when it is fit with access to the first five or more PCs.

RGCs with larger spatial integration exhibit briefer temporal integration of visual input

We next compared the spatial and temporal integration of visual input across all six RGC types. Previous studies in primate and cat examining parasol and midget RGCs or α- and β-RGCs, respectively, have indicated that spatial and temporal integration are inversely related (Frishman et al., 1987; Lee, 1996; Troy and Shou, 2002). Here we examined whether this trend holds in the rodent retina, which has become a dominant model of visual processing (Huberman and Niell, 2011; Sanes and Masland, 2015). Space–time plots of average RFs for each type revealed that types with larger RFs exhibited briefer temporal integration (Fig. 7*A*–*F*). This relationship held across all seven analyzed retinas (Fig. 7*G*). This comparison assumes that the spatiotemporal integration performed by each RGC is well captured by a single spatial filter and a single temporal filter. We checked the degree of independence between the spatial and temporal RFs, where independence is defined as the STA being well approximated by the outer product of a spatial and temporal filter (DeAngelis et al., 1993; Golomb et

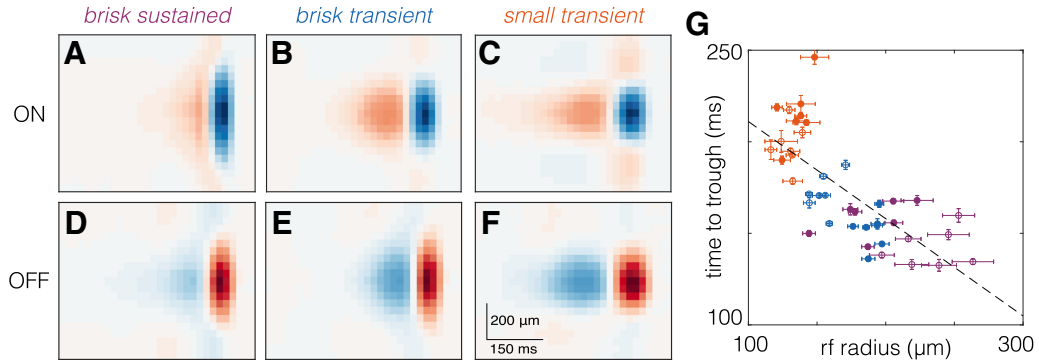

Figure 7. RGC types with larger spatial RFs exhibit briefer temporal RFs. ***A–F***, Average space–time RFs from one retina of ON (***A–C***) and OFF (***D–F***) brisk sustained, brisk transient, and small transient RGCs. ***G***, Comparison of spatial integration (RF radius) to temporal integration (time to trough). Each point corresponds to one RGC type from one retina; filled (open) symbols are OFF (ON) RGCs. Brisk sustained RGCs are purple, brisk transient RGCs are blue, and small transient RGCs are orange. Dashed line is the best fit line to the data (slope = −0.531; *y*-intercept = 264.15 ms). Error bars are the SE.

al., 1994; Cai et al., 1997; Cowan et al., 2016). Singular value decomposition revealed that for each of the six RGC types we examined, >90% of the variance in the STA was captured by the outer product of a single spatial and temporal filter (data not shown). These results indicate that for these RGC types, spatiotemporal integration was well approximated by a single spatial and temporal filter. Furthermore, in the rodent retina, as in other species, larger spatial integration implies briefer temporal integration.

ON/OFF asymmetries in spatial and temporal integration depend on cell type

Previous work has highlighted asymmetries in the size of spatial RFs between ON and OFF cells, with ON cells having larger RFs (Chichilnisky and Kalmar, 2002; Ratliff et al., 2010). To test whether this organization is ubiquitous across ON and OFF pathways in the rodent retina, we compared the size of spatial RFs for each pair of ON and OFF RGC types. Across seven retinas, ON brisk sustained RGCs exhibited larger spatial RFs than OFF brisk sustained RGCs (Fig. 8*A*, purple). However, ON and OFF brisk transient RGCs exhibited the opposite relationship (Fig. 8*A*, blue). Furthermore, ON and OFF small transient cells exhibited nearly identical RF sizes (Fig. 8*A*, orange). These comparisons were based on a two-dimensional Gaussian fit to the spatial RF to identify the radius of a circle with an area equal to that encompassed within 1 SD of the RF (see Materials and Methods). To test that this result did not depend on a parametric description of the RF, we repeated the comparison for the RF area estimated by the number of stimulus pixels that drove an appreciable change in firing rate for each RGC (see Materials and Methods). Qualitatively, the results were unchanged by the nonparametric analysis (Fig. 8*B*). Thus, previously observed asymmetries do not generalize across cell types.

Previous studies have noted asymmetries in the temporal integration between ON and OFF pathways (Chichilnisky, 2001; Pandarinath et al., 2010) Thus, we next compared the duration of temporal integration between ON and OFF pairs. The duration of the temporal integration was estimated by the time-to-zero between the peak and the trough of the temporal RFs. Consistent with previous results, among brisk sustained RGCs, ON cells exhibited briefer temporal integration than OFF cells (Fig. 8*C*, purple). However, the opposite was observed for brisk transient RGCs (Fig. 8*C*, orange). Similar to the results obtained for spatial RFs, ON and OFF small transient cells exhibited similar durations of temporal integration (Figs. 6, 8, orange).

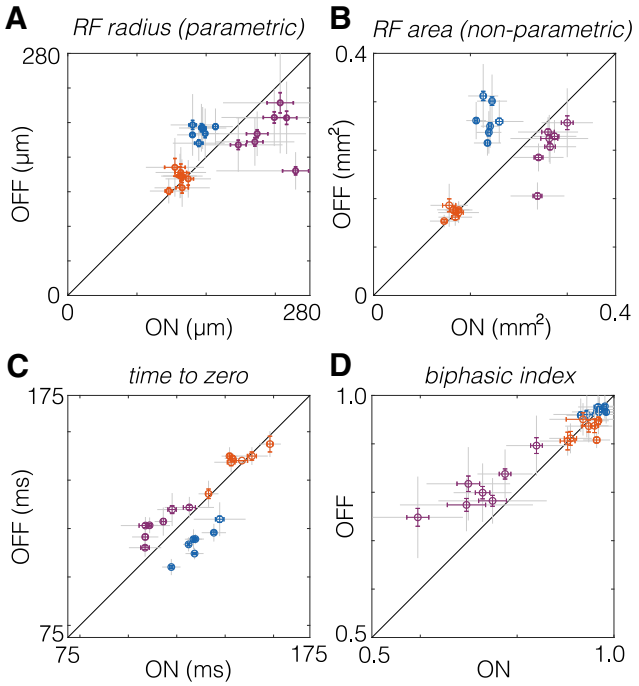

Figure 8. Comparison of spatial and temporal RF properties between ON and OFF RGC pairs. ***A***, Spatial RF radii compared between pairs of ON and OFF RGCs. RF radii were derived from a two-dimensional Gaussian fit to the spatial RF. Brisk sustained RGCs are purple, brisk transient RGCs are blue, and small transient RGCs are orange. Each point shows comparison from one retina. Gray error bars show the SD; color error bars show the SE. ***B***, Same as ***A***, but comparing the RF area estimated nonparametrically from the STA (see Materials and Methods). ***C***, Comparison of temporal integration estimated from the time to zero of the temporal RF (see Materials and Methods). ***D***, Comparison of the biphasic index across pairs of ON and OFF RGCs.

In addition to the duration of temporal integration, RGCs can differ in the dynamics of integration. A key measure of their temporal dynamics is their biphasic index (i.e., degree of transience). For a shift-invariant linear system, the biphasic index indicates key properties of temporal filtering (e.g., low-pass vs bandpass), and it indicates how transient versus sustained the spiking response will be to a prolonged step in light intensity (Field et al., 2007; Petrusca et al., 2007). Higher biphasic indices indicate more strongly bandpass temporal filtering and more transient light responses. Comparing biphasic indices across ON and OFF pairs revealed that among brisk sustained RGCs, OFF

cells exhibited more biphasic temporal integration than ON cells (Fig. 8*D*, purple). However, biphasic indices were similar between ON and OFF cells for brisk and small transient RGCs (Fig. 8*D*, blue and orange). These results indicate that ON/OFF asymmetries in the dynamics of temporal integration are present in some visual pathways, but not all.

Asymmetries in linearity, gain, and signal-to-noise ratio among ON and OFF RGC types

The analyses described above compare the spatial and temporal integration of visual input between ON and OFF RGC types. However, these analyses do not reveal differences in spiking output across cell types. The degree of linearity versus rectification, gain, and signal-to-noise ratio (SNR) in the spiking output are all key features dictating the signals provided to downstream brain areas. Previous work has noted that OFF cells are more strongly rectified in their spiking output than ON cells (Chichilnisky and Kalmar, 2002; Zaghloul et al., 2003; Turner and Rieke, 2016); thus, pathway asymmetries may extend beyond the integration of sensory input.

To characterize and compare the transformation between visual input and spiking output, we estimated static nonlinearities that relate the filtered visual stimulus to the number of spikes produced by each neuron (Fig. 9*A*; Chichilnisky, 2001). These static nonlinearities can be thought of as contrast response functions, where contrast is defined as the similarity between the visual stimulus and the spatiotemporal RF.

ON and OFF brisk sustained RGCs exhibited the most linear contrast response functions (Fig. 9*A*, purple); their spike rates were modulated relatively symmetrically around zero contrast. Brisk transient and small transient cells were progressively more rectified in their spike output (Fig. 9*A*, blue and orange). ON and OFF brisk transient cells exhibited the largest changes in spike rate to large positive or negative contrasts, respectively (Fig. 9*A*, blue).

To relate spiking output to RF properties, we compared RF size to the strength of rectification, as assayed by the nonlinearity (NL) index, which was computed as the log of the ratios of the slope at the maximum generator signal to the slope at zero generator signal (Chichilnisky and Kalmar, 2002). This comparison revealed that cells with smaller RFs were more rectified in their spiking output than cells with larger RFs (Fig. 9*B*). Because temporal integration was inversely related to spatial integration (Fig. 7*G*), longer temporal integration also implied greater rectification in spike output.

To test for asymmetries in the spiking output of ON and OFF cell types, we first examined NL indices, as follows: the logarithm of the ratio of the slope at the maximum to the slope at zero. For brisk sustained and brisk transient RGCs, ON cells had larger NL indices (greater rectification) than OFF cells (Fig. 9*C*, purple and blue). However, this relationship was reversed for small transient RGCs (Fig. 9*C*, orange). Gain, the log of the slope of the contrast response function at zero contrast, was larger among OFF cells than ON cells for brisk sustained and brisk transient cells (Fig. 9*D*, purple and blue), but small transient RGCs exhibited the opposite trend (Fig. 9*D*, orange). Finally, the SNR was compared between ON and OFF pathways. The SNR was defined as the gain (Fig. 9*E*) divided by the SD of the spike rate at zero contrast (Chichilnisky and Kalmar, 2002). Similar to gain, OFF brisk sustained and brisk transient cells exhibited higher SNR than ON cells (Fig. 9*E*, purple and blue). ON small transient cells exhibited a weak tendency toward higher SNR than OFF small transient cells (Fig. 9*E*, orange). Cumulatively, these analyses summarize the relationships in spiking output across three pairs of ON and OFF RGCs and illustrate that each pair exhibits a distinct relationship among the degree of linearity, gain, and SNR.

Discussion

In this study, we distinguished three functionally matched pairs of ON and OFF cells, which provided an opportunity to test the extent to which ON/OFF asymmetries generalize across a greater range of cell types. This comparison results in an expansion of the diversity of asymmetries present in the mammalian retina. Asymmetries between ON and OFF brisk sustained cells were consistent with previous observations. However, ON and OFF brisk transient cells exhibited asymmetries of opposite polarity, and small transient cells exhibited nearly symmetric spatiotemporal integration. Thus, our work alters the conventional view that ON and OFF asymmetries are consistent across diverse RGC types. Below, we comment on the method used to classify RGCs in this study, we suggest correspondences to morphologically defined cell types, and we relate the RF organization of RGCs in this study to that observed in other species.

Functional classifications of rodent RGCs

To functionally classify RGCs, we followed the unsupervised classification approach adopted by several previous studies of RGC diversity (Carcieri et al., 2003; Farrow and Masland, 2011; Baden et al., 2016), with the following differences. The first difference was that RGCs were classified using data from individual recordings instead of pooling data across recordings. This reduced the impact of interexperiment variability, which can either blur distinctions between cell types or cause the identification of too many types. Second, relevant response features that distinguished each type were identified before classification. This improved the performance of the Gaussian mixture model because it produced well separated clusters, thereby minimizing misclassification rates. Only two or three features were selected at each classification step, which kept data requirements for classification relatively low. Third, the classification approach was serial. This mitigated ambiguity in choosing the right number of clusters because each step consisted of fitting just two clusters to the collection of ON cells and two more clusters to the collection of OFF cells (Fig. 2*C–E*). Finally, because many RGCs were recorded in each experiment, this allowed the mosaic arrangement of RFs to provide complementary evidence that the clustered cells were an irreducible type (Wässle et al., 1981b; Devries and Baylor, 1997; Cook and Chalupa, 2000; Field and Chichilnisky, 2007; Anishchenko et al., 2010). Cumulatively, this combination of features facilitated an analysis of the functional organization of six RGC types.

While this approach was reproducible across recordings, it did not classify all recorded cells or identify all of the functional types. Given an RGC density of ~1500 cells/mm^2 in the dorsal region of rat retina targeted in these experiments (Danias et al., 2002), 10–15% of RGCs over the electrode array had well sorted spikes and were tracked across multiple stimulus conditions, which were requirements for the data analyzed here. Among recorded RGCs, 37 ± 3% were not classified because too few cells of other types were sampled. Each stimulus used in this study was presented "full field," which likely attenuated or silenced spiking in at least some RGC types (e.g., local-edge detectors; van Wyk et al., 2006; Zhang et al., 2012). Moreover, only six irreducible RGC types were identified. This falls well short of the ~30 (possibly 40) functionally distinct types that likely exist in the mammalian retina (Field and Chichilnisky, 2007; Völgyi et al., 2009; Sümbül et

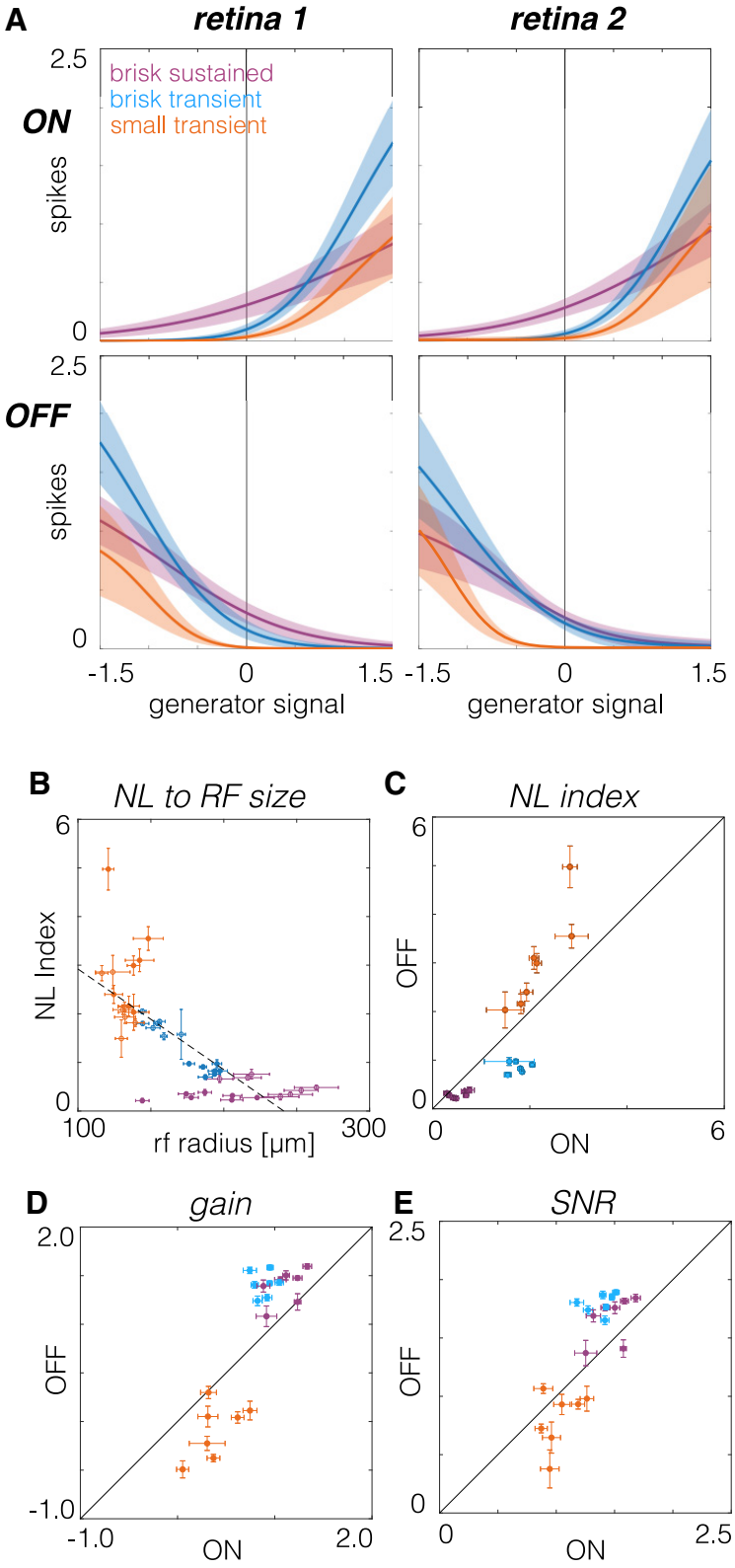

Figure 9. Comparison of contrast response functions across RGC types. ***A***, Contrast response functions estimated from the static nonlinearities that relate visual stimuli filtered by the spatiotemporal RF to mean spike counts. Left and right show data from two retinas; top and bottom show ON and OFF RGCs, respectively. ***B***, Comparison of the nonlinearity index to RF radius. Brisk sustained RGCs are purple, brisk transient RGCs are blue, and small transient RGCs are orange. Filled (open) circles are OFF (ON) cells. ***C***, Nonlinearity index compared between pairs of ON and OFF RGCs. ***D***, Gain compared between pairs of ON and OFF RGCs. ***E***, SNR compared between ON and OFF pairs.

al., 2014; Sanes and Masland, 2015; Baden et al., 2016). A more complete functional classification of RGC types will be facilitated by using a wider variety of stimuli and developing approaches for recording and spike sorting a higher fraction of RGCs over the MEA (Segev et al., 2004; Prentice et al., 2011; Marre et al., 2012; Yger et al., 2018).

Correspondences to morphologically defined RGC types

A major goal in retinal research is to generate a complete catalog of RGCs that specifies the correspondences among their function, morphology, and projections to the brain (Sanes and Masland, 2015). We did not determine the morphology of the recorded RGCs; however, their RF sizes and response kinetics provide some plausible correspondences. The six RGC types examined here all had relatively large RFs and large well isolated spikes on the MEA. These features indicate large dendritic fields and relatively large somas, suggesting correspondences to the A and C groups of RGCs identified by Sun et al. (2002). The brisk sustained and brisk transient cells likely correspond to the δ- and α-cells identified by Peichl (1989). The ON and OFF small transient cells likely have smaller cell bodies and dendrites in the interior of the inner plexiform layer (IPL) because of their transient response properties (Borghuis et al., 2013), suggesting correspondences to the outer and inner B1 RGCs (Huxlin and Goodchild, 1997). We emphasize that these are hypothesized correspondences that require additional experiments to test.

Diverse contrast response functions across RGC types

The contrast response functions (i.e., static nonlinearities) associated with each RGC type differed significantly across the six types we analyzed (Fig. 9). Brisk sustained cells were the most linear, while small transient cells were the most rectified in their output. This trend was present across both ON and OFF types. The degree of rectification in RGC output has been largely attributed to rectification in the excitatory synaptic inputs provided by bipolar cells (Zaghloul et al., 2003; Schwartz et al., 2012; Borghuis et al., 2013; Turner and Rieke, 2016). This predicts that the different bipolar cells feeding these distinct RGC types exhibit differing degrees of rectification in their output. These differences are likely shaped by inhibitory amacrine cells (Franke et al., 2017). Importantly, differences in this

rectification can play a substantial role in tuning how different cell types respond to natural scenes (Turner and Rieke, 2016).

Mechanisms and downstream implications of functional asymmetries

Asymmetries between ON and OFF pathways have been observed across a range of species and contexts. Among primate parasol RGCs, ON cells exhibit larger RFs, briefer temporal integration, and more linear contrast response functions than OFF cells (Chichilnisky and Kalmar, 2002). Some of these asymmetries have been observed in other species and cell types. For example, α-cells in guinea pigs and brisk sustained cells in rabbits exhibit at least some overlapping asymmetries (Zaghloul et al., 2003; Ratliff et al., 2010; Buldyrev and Taylor, 2013).

The mechanisms that produce some of these asymmetries are clear. For example, systematic differences in spatial RF size likely reflect systematic differences in dendritic field size between some ON and OFF RGC types (Peichl et al., 1987; Dacey and Petersen, 1992; Tauchi et al., 1992; Ratliff et al., 2010). Asymmetries in contrast response functions between ON and OFF α-cells reflect differences in baseline transmitter release from presynaptic bipolar cells (Zaghloul et al., 2003). Furthermore, differences in intrinsic cellular conductances and synaptic inputs conspire to yield differences in spontaneous firing, spatial nonlinearities, and other properties (Murphy and Rieke, 2006; Margolis and Detwiler, 2007; Zhang and Diamond, 2009; Buldyrev and Taylor, 2013; Turner and Rieke, 2016).

One question raised by these observations is the extent to which these asymmetries meaningfully shape downstream visual processing and perception. Asymmetries in ON and OFF responses originating in the retina clearly influence signals in LGN (Jiang et al., 2015) and shape the responses in primary visual cortex (Yeh et al., 2009; Jin et al., 2011; Komban et al., 2014; Lee et al., 2016). Furthermore, these asymmetries likely underlie psychophysical asymmetries between sensing and processing increments versus decrements of light (Pons et al., 2017).

Why do ON/OFF pathways exhibit diverse contrast response functions and asymmetries?

Several recent studies have also examined the benefit of distinct contrast response functions for encoding, and how these functions can be optimized given the constraints imposed by different sources of noise within the retina. One benefit of diverse contrast response functions for encoding is that they could serve to decorrelate a population of neurons responding to complex stimuli. This decorrelation can reduce redundancy in the population code, thereby transmitting the same information with fewer spikes (Barlow, 1961; Vinje and Gallant, 2000; Pitkow and Meister, 2012). Alternatively, different nonlinearities may reflect compensation for noise at different stages of retinal processing to achieve efficient coding (Brinkman et al., 2016). For example, if the dominant source of noise is present before rectification, the most efficient coding is achieved by relatively linear contrast response functions, while more strongly rectified functions are preferred when noise dominates after rectification. Determining how the contrast response functions we observed either serve or constrain the encoding of natural scenes across six parallel processing streams is an important direction for future work.

Several studies have also indicated that ON/OFF asymmetries are optimizations to the statistics of natural scenes. First, a theoretical analysis indicates that the division of processing ON and OFF signals transmits more information with fewer spikes than alternative encoding strategies (Gjorgjieva et al., 2014). Second, the observation that at least some OFF pathways have smaller RFs than ON cells may allow the retina to transmit more information about natural scenes, which exhibit more regions of relative darkness (Ratliff et al., 2010). Similarly, several asymmetries can be predicted by applying efficient coding theory to natural scenes (Karklin and Simoncelli, 2011; Doi et al., 2012).

Given that previous work suggests that natural scenes and efficient coding can predict one set of asymmetries (e.g., ON cells having larger spatial RFs than OFF cells), why do different pathways exhibit different asymmetries? One possibility comes from a recent analysis of the spatial frequency distribution of light and dark asymmetries in natural scenes (Cooper and Norcia, 2015). This work shows that intensity distributions are skewed toward darker values at low spatial frequencies, but not at higher spatial frequencies. This may explain why cell types with the smallest RFs in this study exhibited nearly equivalent spatiotemporal integration (Fig. 8). Two other considerations may be important as well. First, previous analyses of natural scenes have largely focused on static images, not on natural movies, or movies that consider head and eye movements. These temporal dynamics may interact with the differences in temporal integration across RGC types to cause different asymmetries to be optimal. Second, previous analyses have largely focused on just two pathways, one ON and one OFF (Karklin and Simoncelli, 2011). It is unclear that the conclusions for encoding natural scenes under this context will generalize if a system has more pathways to use for encoding visual scenes. To resolve these possibilities, a more complete analysis of the interactions between natural movies (including head and eye movements; Wallace et al., 2013) and the spatiotemporal dynamics of RGC RFs will be required.

References

Ala-Laurila P, Rieke F (2014) Coincidence detection of single-photon responses in the inner retina at the sensitivity limit of vision. Curr Biol 24:2888–2898. CrossRef Medline

Anishchenko A, Greschner M, Elstrott J, Sher A, Litke AM, Feller MB, Chichilnisky EJ (2010) Receptive field mosaics of retinal ganglion cells are established without visual experience. J Neurophysiol 103:1856–1864. CrossRef Medline

Baden T, Berens P, Franke K, Román Rosón M, Bethge M, Euler T (2016) The functional diversity of retinal ganglion cells in the mouse. Nature 529:345–350. CrossRef Medline

Barlow H (1961) Possible principles underlying the transformation of sensory messages. In: Sensory communication (Rosenblith W, ed), pp 217–234. Cambridge, MA: MIT.

Berman NJ, Maler L (1998) Inhibition evoked from primary afferents in the electrosensory lateral line lobe of the weakly electric fish (Apteronotus leptorhynchus). J Neurophysiol 80:3173–3196. CrossRef Medline

Borghuis BG, Marvin JS, Looger LL, Demb JB (2013) Two-photon imaging of nonlinear glutamate release dynamics at bipolar cell synapses in the mouse retina. J Neurosci 33:10972–10985. CrossRef Medline

Brinkman BA, Weber AI, Rieke F, Shea-Brown E (2016) How do efficient coding strategies depend on origins of noise in neural circuits? PLoS Comput Biol 12:e1005150. CrossRef Medline

Buldyrev I, Taylor WR (2013) Inhibitory mechanisms that generate centre and surround properties in ON and OFF brisk-sustained ganglion cells in the rabbit retina. J Physiol 591:303–325. CrossRef Medline

Burgstaller M, Tichy H (2011) Functional asymmetries in cockroach ON and OFF olfactory receptor neurons. J Neurophysiol 105:834–845. CrossRef Medline

Cai D, DeAngelis GC, Freeman RD (1997) Spatiotemporal receptive field organization in the lateral geniculate nucleus of cats and kittens. J Neurophysiol 78:1045–1061. CrossRef Medline

Caldwell JH, Daw NW (1978) New properties of rabbit retinal ganglion cells. J Physiol 276:257–276. CrossRef Medline

Carcieri SM, Jacobs AL, Nirenberg S (2003) Classification of retinal ganglion cells: a statistical approach. J Neurophysiol 90:1704–1713. CrossRef Medline

Chichilnisky EJ (2001) A simple white noise analysis of neuronal light responses. Network 12:199–213. CrossRef Medline
Chichilnisky EJ, Kalmar RS (2002) Functional asymmetries in ON and OFF ganglion cells of primate retina. J Neurosci 22:2737–2747. CrossRef Medline
Clarke SE, Longtin A, Maler L (2014) A neural code for looming and receding motion is distributed over a population of electrosensory ON and OFF contrast cells. J Neurosci 34:5583–5594. CrossRef Medline
Cleland BG, Levick WR (1974) Brisk and sluggish concentrically organized ganglion cells in the cat's retina. J Physiol 240:421–456. CrossRef Medline
Cleland BG, Levick WR, Wässle H (1975) Physiological identification of a morphological class of cat retinal ganglion cells. J Physiol 248:151–171. CrossRef Medline
Cook JE, Chalupa LM (2000) Retinal mosaics: new insights into an old concept. Trends Neurosci 23:26–34. CrossRef Medline
Cooper EA, Norcia AM (2015) Predicting cortical dark/bright asymmetries from natural image statistics and early visual transforms. PLoS Comput Biol 11:e1004268. CrossRef Medline
Cowan CS, Sabharwal J, Wu SM (2016) Space-time codependence of retinal ganglion cells can be explained by novel and separable components of their receptive fields. Physiol Rep 4:e12952. CrossRef Medline
Crook JD, Peterson BB, Packer OS, Robinson FR, Troy JB, Dacey DM (2008a) Y-cell receptive field and collicular projection of parasol ganglion cells in macaque monkey retina. J Neurosci 28:11277–11291. CrossRef Medline
Dacey DM (1993) The mosaic of midget ganglion cells in the human retina. J Neurosci 13:5334–5355. CrossRef Medline
Dacey D (2004) Origins of perception: retinal ganglion cell diversity and the creation of parallel visual pathways. In: The cognitive neurosciences (Gazzaniga MS, ed), pp 281–301. Cambridge, MA: MIT.
Dacey DM, Petersen MR (1992) Dendritic field size and morphology of midget and parasol ganglion cells of the human retina. Proc Natl Acad Sci U S A 89:9666–9670. CrossRef Medline
Danias J, Shen F, Goldblum D, Chen B, Ramos-Esteban J, Podos SM, Mittag T (2002) Cytoarchitecture of the retinal ganglion cells in the rat. Invest Ophthalmol Vis Sci 43:587–594. Medline
DeAngelis GC, Ohzawa I, Freeman RD (1993) Spatiotemporal organization of simple-cell receptive fields in the cat's striate cortex. II. linearity of temporal and spatial summation. J Neurophysiol 69:1118–1135. CrossRef Medline
DeVries SH, Baylor DA (1995) An alternative pathway for signal flow from rod photoreceptors to ganglion cells in mammalian retina. Proc Natl Acad Sci U S A 92:10658–10662. CrossRef Medline
Devries SH, Baylor DA (1997) Mosaic arrangement of ganglion cell receptive fields in rabbit retina. J Neurophysiol 78:2048–2060. CrossRef Medline
Doi E, Gauthier JL, Field GD, Shlens J, Sher A, Greschner M, Machado TA, Jepson LH, Mathieson K, Gunning DE, Litke AM, Paninski L, Chichilnisky EJ, Simoncelli EP (2012) Efficient coding of spatial information in the primate retina. J Neurosci 32:16256–16264. CrossRef Medline
Elstrott J, Anishchenko A, Greschner M, Sher A, Litke AM, Chichilnisky EJ, Feller MB (2008) Direction selectivity in the retina is established independent of visual experience and cholinergic retinal waves. Neuron 58:499–506. CrossRef Medline
Farrow K, Masland RH (2011) Physiological clustering of visual channels in the mouse retina. J Neurophysiol 105:1516–1530. CrossRef Medline
Field GD, Chichilnisky EJ (2007) Information processing in the primate retina: circuitry and coding. Annu Rev Neurosci 30:1–30. CrossRef Medline
Field GD, Sher A, Gauthier JL, Greschner M, Shlens J, Litke AM, Chichilnisky EJ (2007) Spatial properties and functional organization of small bistratified ganglion cells in primate retina. J Neurosci 27:13261–13272. CrossRef Medline
Field GD, Greschner M, Gauthier JL, Rangel C, Shlens J, Sher A, Marshak DW, Litke AM, Chichilnisky EJ (2009) High-sensitivity rod photoreceptor input to the blue-yellow color opponent pathway in macaque retina. Nat Neurosci 12:1159–1164. CrossRef Medline
Franke K, Berens P, Schubert T, Bethge M, Euler T, Baden T (2017) Inhibition decorrelates visual feature representations in the inner retina. Nature 542:439–444. CrossRef Medline
Frechette ES, Sher A, Grivich MI, Petrusca D, Litke AM, Chichilnisky EJ (2005) Fidelity of the ensemble code for visual motion in primate retina. J Neurophysiol 94:119–135. CrossRef Medline
Freeman J, Field GD, Li PH, Greschner M, Gunning DE, Mathieson K, Sher A, Litke AM, Paninski L, Simoncelli EP, Chichilnisky EJ (2015) Mapping nonlinear receptive field structure in primate retina at single cone resolution. Elife 4:e05241. CrossRef Medline
Frishman LJ, Freeman AW, Troy JB, Schweitzer-Tong DE, Enroth-Cugell C (1987) Spatiotemporal frequency responses of cat retinal ganglion cells. J Gen Physiol 89:599–628. CrossRef Medline
Gauthier JL, Field GD, Sher A, Shlens J, Greschner M, Litke AM, Chichilnisky EJ (2009) Uniform signal redundancy of parasol and midget ganglion cells in primate retina. J Neurosci 29:4675–4680. CrossRef Medline
Girman S, Lund R (2010) Orientation-specific modulation of rat retinal ganglion cell responses and its dependence on relative orientations of the center and surround gratings. J Neurophysiol 104:2951–2962. CrossRef Medline
Gjorgjieva J, Sompolinsky H, Meister M (2014) Benefits of pathway splitting in sensory coding. J Neurosci 34:12127–12144. CrossRef Medline
Golomb D, Kleinfeld D, Reid RC, Shapley RM, Shraiman BI (1994) On temporal codes and the spatiotemporal response of neurons in the lateral geniculate nucleus. J Neurophysiol 72:2990–3003. CrossRef Medline
Hartline H (1938) The response of single optic nerve fibers of the vertebrate eye to illumination of the retina. Am J Physiol 121:400–415.
Heine WF, Passaglia CL (2011) Spatial receptive field properties of rat retinal ganglion cells. Vis Neurosci 28:403–417. CrossRef Medline
Hochstein S, Shapley RM (1976) Linear and nonlinear spatial subunits in Y cat retinal ganglion cells. J Physiol 262:265–284. CrossRef Medline
Hubel DH, Wiesel TN (1962) Receptive fields, binocular interaction and functional architecture in the cat's visual cortex. J Physiol 160:106–154. CrossRef Medline
Huberman AD, Niell CM (2011) What can mice tell us about how vision works? Trends Neurosci 34:464–473. CrossRef Medline
Huxlin KR, Goodchild AK (1997) Retinal ganglion cells in the albino rat: revised morphological classification. J Comp Neurol 385:309–323. CrossRef Medline
Jiang Y, Purushothaman G, Casagrande VA (2015) The functional asymmetry of ON and OFF channels in the perception of contrast. J Neurophysiol 114:2816–2829. CrossRef Medline
Jin J, Wang Y, Lashgari R, Swadlow HA, Alonso JM (2011) Faster thalamocortical processing for dark than light visual targets. J Neurosci 31:17471–17479. CrossRef Medline
Karklin Y, Simoncelli EP (2011) Efficient coding of natural images with a population of noisy linear-nonlinear neurons. Adv Neural Inf Process Syst 24:999–1007. Medline
Keat J, Reinagel P, Reid RC, Meister M (2001) Predicting every spike: a model for the responses of visual neurons. Neuron 30:803–817. CrossRef Medline
Komban SJ, Kremkow J, Jin J, Wang Y, Lashgari R, Li X, Zaidi Q, Alonso JM (2014) Neuronal and perceptual differences in the temporal processing of darks and lights. Neuron 82:224–234. CrossRef Medline
Kuffler SW (1953) Discharge patterns and functional organization of mammalian retina. J Neurophysiol 16:37–68. CrossRef Medline
Lee BB (1996) Receptive field structure in the primate retina. Vision Res 36:631–644. CrossRef Medline
Lee KS, Huang X, Fitzpatrick D (2016) Topology of ON and OFF inputs in visual cortex enables an invariant columnar architecture. Nature 533:90–94. CrossRef Medline
Litke A, Bezayiff N, Chichilnisky E, Cunningham W, Dabrowski W, Grillo A, Grivich M, Grybos P, Hottowy P, Kachiguine S (2004) What does the eye tell the brain? Development of a system for the large-scale recording of retinal output activity. IEEE Trans Nucl Sci 51:1434–1440. CrossRef
Margolis DJ, Detwiler PB (2007) Different mechanisms generate maintained activity in ON and OFF retinal ganglion cells. J Neurosci 27:5994–6005. CrossRef Medline
Marre O, Amodei D, Deshmukh N, Sadeghi K, Soo F, Holy TE, Berry MJ 2nd (2012) Mapping a complete neural population in the retina. J Neurosci 32:14859–14873. CrossRef Medline
Murphy GJ, Rieke F (2006) Network variability limits stimulus-evoked spike timing precision in retinal ganglion cells. Neuron 52:511–524. CrossRef Medline
Nirenberg S, Bomash I, Pillow JW, Victor JD (2010) Heterogeneous re-

sponse dynamics in retinal ganglion cells: the interplay of predictive coding and adaptation. J Neurophysiol 103:3184–3194. CrossRef Medline
Novelli E, Resta V, Galli-Resta L (2005) Mechanisms controlling the formation of retinal mosaics. Prog Brain Res 147:141–153. CrossRef Medline
Pandarinath C, Victor JD, Nirenberg S (2010) Symmetry breakdown in the ON and OFF pathways of the retina at night: functional implications. J Neurosci 30:10006–10014. CrossRef Medline
Peichl L (1989) Alpha and delta ganglion cells in the rat retina. J Comp Neurol 286:120–139. CrossRef Medline
Peichl L, Buhl EH, Boycott BB (1987) Alpha ganglion cells in the rabbit retina. J Comp Neurol 263:25–41. CrossRef Medline
Petrusca D, Grivich MI, Sher A, Field GD, Gauthier JL, Greschner M, Shlens J, Chichilnisky EJ, Litke AM (2007) Identification and characterization of a Y-like primate retinal ganglion cell type. J Neurosci 27:11019–11027. CrossRef Medline
Pillow JW, Paninski L, Uzzell VJ, Simoncelli EP, Chichilnisky EJ (2005) Prediction and decoding of retinal ganglion cell responses with a probabilistic spiking model. J Neurosci 25:11003–11013. CrossRef Medline
Pitkow X, Meister M (2012) Decorrelation and efficient coding by retinal ganglion cells. Nat Neurosci 15:628–635. CrossRef Medline
Pons C, Mazade R, Jin J, Dul MW, Zaidi Q, Alonso JM (2017) Neuronal mechanisms underlying differences in spatial resolution between darks and lights in human vision. J Vis 17(14):5, 1–24. CrossRef Medline
Prentice JS, Homann J, Simmons KD, Tkačik G, Balasubramanian V, Nelson PC (2011) Fast, scalable, Bayesian spike identification for multi-electrode arrays. PLoS One 6:e19884. CrossRef Medline
Ratliff CP, Borghuis BG, Kao YH, Sterling P, Balasubramanian V (2010) Retina is structured to process an excess of darkness in natural scenes. Proc Natl Acad Sci U S A 107:17368–17373. CrossRef Medline
Rivlin-Etzion M, Wei W, Feller MB (2012) Visual stimulation reverses the directional preference of direction-selective retinal ganglion cells. Neuron 76:518–525. CrossRef Medline
Sanes JR, Masland RH (2015) The types of retinal ganglion cells: current status and implications for neuronal classification. Annu Rev Neurosci 38:221–246. CrossRef Medline
Scholl B, Pattadkal JJ, Rowe A, Priebe NJ (2017) Functional characterization and spatial clustering of visual cortical neurons in the predatory grasshopper mouse onychomys arenicola. J Neurophysiol 117:910–918. CrossRef Medline
Schwartz GW, Okawa H, Dunn FA, Morgan JL, Kerschensteiner D, Wong RO, Rieke F (2012) The spatial structure of a nonlinear receptive field. Nat Neurosci 15:1572–1580. CrossRef Medline
Segev R, Goodhouse J, Puchalla J, Berry MJ 2nd (2004) Recording spikes from a large fraction of the ganglion cells in a retinal patch. Nat Neurosci 7:1154–1161. CrossRef Medline
Shlens J, Field GD, Gauthier JL, Grivich MI, Petrusca D, Sher A, Litke AM, Chichilnisky EJ (2006) The structure of multi-neuron firing patterns in primate retina. J Neurosci 26:8254–8266. CrossRef Medline
Sümbül U, Song S, McCulloch K, Becker M, Lin B, Sanes JR, Masland RH, Seung HS (2014) A genetic and computational approach to structurally classify neuronal types. Nat Commun 5:3512. CrossRef Medline
Sun W, Li N, He S (2002) Large-scale morphological survey of rat retinal ganglion cells. Vis Neurosci 19:483–493. CrossRef Medline
Tauchi M, Morigiwa K, Fukuda Y (1992) Morphological comparisons between outer and inner ramifying alpha cells of the albino rat retina. Exp Brain Res 88:67–77. CrossRef Medline
Troy JB, Shou T (2002) The receptive fields of cat retinal ganglion cells in physiological and pathological states: where we are after half a century of research. Prog Retin Eye Res 21:263–302. CrossRef Medline
Turner MH, Rieke F (2016) Synaptic rectification controls nonlinear spatial integration of natural visual inputs. Neuron 90:1257–1271. CrossRef Medline
van Wyk M, Taylor WR, Vaney DI (2006) Local edge detectors: a substrate for fine spatial vision at low temporal frequencies in rabbit retina. J Neurosci 26:13250–13263. CrossRef Medline
Vinje WE, Gallant JL (2000) Sparse coding and decorrelation in primary visual cortex during natural vision. Science 287:1273–1276. CrossRef Medline
Völgyi B, Chheda S, Bloomfield SA (2009) Tracer coupling patterns of the ganglion cell subtypes in the mouse retina. J Comp Neurol 512:664–687. CrossRef Medline
Wallace DJ, Greenberg DS, Sawinski J, Rulla S, Notaro G, Kerr JN (2013) Rats maintain an overhead binocular field at the expense of constant fusion. Nature 498:65–69. CrossRef Medline
Wässle H, Boycott BB (1991) Functional architecture of the mammalian retina. Physiol Rev 71:447–480. CrossRef Medline
Wässle H, Riemann HJ (1978) The mosaic of nerve cells in the mammalian retina. Proc R Soc Lond B Biol Sci 200:441–461. CrossRef Medline
Wässle H, Peichl L, Boycott BB (1981a) Morphology and topography of on- and off-alpha cells in the cat retina. Proc R Soc Lond B Biol Sci 212:157–175. CrossRef Medline
Wässle H, Peichl L, Boycott BB (1981b) Dendritic territories of cat retinal ganglion cells. Nature 292:344–345. CrossRef Medline
Watanabe M, Rodieck RW (1989) Parasol and midget ganglion cells of the primate retina. J Comp Neurol 289:434–454. CrossRef Medline
Yeh CI, Xing D, Shapley RM (2009) "Black" responses dominate macaque primary visual cortex V1. J Neurosci 29:11753–11760. CrossRef Medline
Yger P, Spampinato GL, Esposito E, Lefebvre B, Deny S, Gardella C, Stimberg M, Jetter F, Zeck G, Picaud S, Duebel J, Marre O (2018) A spike sorting toolbox for up to thousands of electrodes validated with ground truth recordings in vitro and in vivo. Elife 7:e34518. CrossRef Medline
Yu WQ, Grzywacz NM, Lee EJ, Field GD (2017) Cell type-specific changes in retinal ganglion cell function induced by rod death and cone reorganization in rats. J Neurophysiol 118:434–454. CrossRef Medline
Zaghloul KA, Boahen K, Demb JB (2003) Different circuits for ON and OFF retinal ganglion cells cause different contrast sensitivities. J Neurosci 23:2645–2654. CrossRef Medline
Zhang J, Diamond JS (2009) Subunit- and pathway-specific localization of NMDA receptors and scaffolding proteins at ganglion cell synapses in rat retina. J Neurosci 29:4274–4286. CrossRef Medline
Zhang Y, Kim IJ, Sanes JR, Meister M (2012) The most numerous ganglion cell type of the mouse retina is a selective feature detector. Proc Natl Acad Sci U S A 109:E2391–E2398. CrossRef Medline